

1 **A study on some basic features of inertial oscillations**  
2 **and near-inertial internal waves**

3 Shengli Chen, Daoyi Chen, and Jiuxing Xing

4 Shenzhen Key Laboratory for Coastal Ocean Dynamic and Environment, Graduate School at  
5 Shenzhen, Tsinghua University, Shenzhen 518055, China.

6 *Correspondence to:* Jiuxing Xing ([jxx2012@sz.tsinghua.edu.cn](mailto:jxx2012@sz.tsinghua.edu.cn))

7

8

9

10

11

12

13

14

15

16

17

18

19

20

21

22

23 **Abstract**

24 Some basic features of inertial oscillations and near-inertial internal waves are investigated by simulating  
25 a two-dimensional ( $x$ - $z$ ) rectangular basin ( $300 \text{ km} \times 60 \text{ m}$ ) driven by a wind pulse. For the homogeneous  
26 case, near-inertial motions are pure inertial oscillations. The inertial oscillation shows typical opposite  
27 currents between surface and lower layers, which is formed by the feedback between barotropic waves  
28 and inertial currents. For the stratified case, near-inertial internal waves are generated at land boundaries  
29 and propagate offshore with higher frequencies, which induce tilting of velocity contours in the  
30 thermocline. The inertial oscillation is uniform across the whole basin, except near the coastal boundaries  
31 ( $\sim 20 \text{ km}$ ) where it quickly declines to zero. This boundary effect is related to great enhancement of  
32 nonlinear terms, especially the vertical nonlinear term ( $w \partial \mathbf{u} / \partial z$ ). With the inclusion of near-inertial  
33 internal waves, the total near-inertial energy has a slight change, with occurrence of a small peak at  $\sim 50$   
34 km, which is similar to previous researches. We conclude that, for this distribution of near-inertial energy,  
35 the boundary effect for inertial oscillations is primary, and the near-inertial internal wave plays a  
36 secondary role. Homogeneous cases with various water depths (50 m, 40 m, 30 m, 20 m) are also  
37 simulated. It is found near-inertial energy monotonously declines with decreasing water depth, because  
38 more energy of the initial wind-driven currents is transferred to seiches by barotropic waves. For the case  
39 of 20 m, the seiches energy even slightly exceeds the near-inertial energy. We suppose this is an important  
40 reason why near-inertial motions are weak and hardly observed in coastal regions.

41

42 **Keywords:** inertial oscillations, near-inertial internal waves, near-inertial energy

43

44

45

46

47

48

## 49 1. Introduction

50 Near-inertial motions have been observed and reported in many seas (e.g. Alford et al., 2016; Webster,  
51 1968). They are mainly generated by changing winds at the sea surface (Pollard and Millard, 1970; Chen  
52 et al., 2015b). The passage of a cyclone or a front can induce very strong near-inertial motions (D'Asaro,  
53 1985), which can last for 1-2 weeks and reach a maximum velocity magnitude of 0.5-1.0 m/s (Chen et  
54 al., 2015a; Zheng et al., 2006; Sun et al., 2011). In deep seas, the near-inertial internal wave propagates  
55 downwards to transfer energy to depth (Leaman and Sanford, 1975; Fu, 1981; Gill, 1984; Alford et al.,  
56 2012). The strong vertical shear of near-inertial currents may play an important role in inducing mixing  
57 across the thermocline (Price, 1981; Burchard and Rippeth, 2009; Chen et al., 2016).

58 In shelf seas, near-inertial motions exhibit a two-layer structure, with an opposite phase between currents  
59 in the surface and lower layers (Malone, 1968; Millot and Crepon, 1981; MacKinnon and Gregg, 2005).  
60 By solving a two-layer analytic model using the Laplace transform, Pettigrew (1981) found this  
61 'baroclinic' structure can be formed by inertial oscillations without inclusion of near-inertial internal  
62 waves. Due to similar vertical structures and frequencies, inertial oscillations and near-inertial internal  
63 waves are hardly separable, and could easily be mistakenly recognized as each other.

64 In shelf seas, the near-inertial energy increases gradually offshore, and reaches a maximum near the shelf  
65 break, found both in observations (Chen et al., 1996) and model simulations (Xing et al., 2004; Nicholls  
66 et al., 2012). Chen and Xie (1997) reproduced this cross-shelf variation both in linear and nonlinear  
67 simulations, and attribute it to large values of the cross-shelf gradient of surface elevation and the vertical  
68 gradient of Reynolds stress near the shelf break. By using the analytic model of Pettigrew (1981),  
69 Shearman (2005) argued that the cross-shelf variation is controlled by baroclinic waves which emanate  
70 from the coast to introduce nullifying effects on the near-inertial energy near shore. Kundu et al. (1983)  
71 found a coastal inhibition of near-inertial energy within the Rossby radius from the coast, which is  
72 attributed to leaking of near-inertial energy downward and offshore. As many factors seem to work, the  
73 mechanism controlling the cross-shelf variation of near-inertial energy is not clear.

74 In this paper, simple two-dimensional simulations are used to investigate some basic features of near-  
75 inertial motions. Cases with and without vertical stratification are simulated to examine properties and  
76 differences between inertial oscillations and near-inertial internal waves. The horizontal distribution of

77 near-inertial energy is discussed in detail. Also cases with various water depths are simulated to  
78 investigate the dependence of near-inertial motions on the water depth.

## 79 **2. Model Settings**

80 The simulated region is a two-dimensional shallow rectangular basin (300 km × 60 m). Numerical  
81 simulations are done by the MIT general circulation model (MITgcm) (Marshall et al., 1997), which  
82 discretizes the primitive equations and can be designed to model a wide range of phenomena. There are  
83 1500 grid points in the horizontal ( $\Delta x = 200$  m) and 60 grid points in vertical ( $\Delta z = 1$  m). The water  
84 depth is uniform, with east and west sides being land boundaries. The vertical and horizontal eddy  
85 viscosities are assumed constant as  $5 \times 10^{-4}$  m<sup>2</sup>/s and 10 m<sup>2</sup>/s, respectively. The Coriolis parameter is  $5 \times 10^{-5}$   
86 s<sup>-1</sup> (at a latitude of 20.11° N). The bottom boundary is no-slip. The model is forced by a spatially uniform  
87 wind which is kept westward and increases from 0 to 0.73 N/m<sup>2</sup> (corresponding to a wind speed of 20  
88 m/s) for the first three hours and then suddenly stops. The model runs for 200 hours in total, with a time  
89 step of 4 seconds. The first case is homogeneous, while the second one has a stratification of two-layer  
90 structure initially. For the stratified case, the temperature is 20°C in the upper layer ( $-30 \text{ m} < z < 0$ ), and  
91 15°C in the lower layer ( $-60 \text{ m} < z < -30 \text{ m}$ ). The salinity is constant, and the density is linearly determined  
92 by the temperature, with an expansion coefficient of  $2 \times 10^{-4}$  °C<sup>-1</sup>. The barotropic and baroclinic Rossby  
93 radii are 485 km and 8 km, respectively.

## 94 **3. Inertial oscillations**

95 The first case is without the presence of vertical stratification. Thus the near-inertial internal wave is  
96 absent, and the near-inertial motion is a pure inertial oscillation.

### 97 **3.1 Vertical structures**

98 The model simulated velocities (Fig. 1) vary near the inertial period (34.9 hours). Spectra of velocities  
99 (not shown) indicate maximum peaks located exactly at the inertial period. The spectra of  $u$  also have a  
100 smaller peak at the period of the first mode seiche (6.9 hours). As this simulation is two-dimensional,  
101 i.e., the gradient along  $y$ -axis is zero, the  $u/v$  of seiche have a value of  $\omega_n/f$  (equals 5 for the first mode  
102 seiche). Thus there is little energy of seiche in  $v$  which shows clearly regular variation at the inertial  
103 frequency.

104 In the vertical direction, currents display a two-layer structure, with their phase being opposite between

105 surface and lower layers. They are maximum at the surface, and have a weaker maximum in the lower  
106 layer (~40 m), with a minimum at the depth of ~20 m. The velocity gradually diminishes to zero at the  
107 bottom due to the bottom friction. This is the typical vertical structure of shelf-sea inertial oscillations,  
108 which have been frequently observed (Shearman, 2005; MacKinnon and Gregg, 2005). In practice, this  
109 vertical distribution can be modified due to presence of other processes, such as the surface maximum  
110 being pushed down to the subsurface (e.g. Chen et al., 2015a). Note that without stratification in this  
111 simulation the near-inertial internal wave is absent. However, this two-layer structure of inertial  
112 oscillations looks ‘baroclinic’, which makes it easy to be mistakenly attributed to the near-inertial internal  
113 wave (Pettigrew, 1981).

114 It is interesting that currents of non-baroclinic inertial oscillations reverse between the surface and lower  
115 layers. This is usually due to the presence of the coast, which requires the normal-to-coast transport to  
116 be zero, thus currents in upper and lower layers compensate each other (e.g., Millot and Crepon, 1981;  
117 Chen et al., 1996). However, it is interesting to see how this vertical structure is established step by step.

118 As the westward wind blows for the first three hours, the initial inertial current is also westward and only  
119 exists in the very surface layer (Fig. 2). In the lower layer there is no movement initially. Thus a westward  
120 transport is produced, which generates a rise (in the west) and fall (in the east) of elevation near land  
121 boundaries. The elevation slope behaves in a form of barotropic wave which propagates offshore at a  
122 large speed (87 km/h). The current driven by the barotropic wave is eastward, and uniform vertically.  
123 Therefore, with the arrival of the barotropic wave the westward current in the surface is reduced, and the  
124 eastward movement in the lower layer commences (Fig. 2). After the passage of the first two barotropic  
125 waves (originated from both sides), currents in the lower layer have reached a relatively large value,  
126 while currents in the surface layer have largely decreased (Fig. 3a). Accordingly, the depth-integrated  
127 transport diminishes significantly. This is a feedback between inertial currents and barotropic waves. If  
128 only the depth-integrated transport of currents exist, barotropic waves will be generated, which reduce  
129 the surface currents but increase the lower layer currents, and thus reduces the current transport. It will  
130 end up with inertial currents in the surface and lower layers having opposite directions and comparable  
131 amplitudes. As seen from Fig. 1b, the typical vertical structure of inertial currents is established within  
132 the first inertial period.

### 133 **3.2 Horizontal distributions of inertial energy**

134 The inertial velocities are almost entirely the same across the basin (Fig. 4), except near the land  
135 boundaries. This indicates that inertial oscillations have a coherence scale of almost the basin width. This  
136 is because in our simulation the wind force is spatially uniform, and the bottom is flat. The inertial  
137 velocities in the lower layer have slightly more variation across the basin than those in the surface layer,  
138 because inertial velocities in the lower layer depend on the propagation of barotropic waves as discussed  
139 in 3.1, while the surface inertial currents are driven by spatially uniform wind. In shelf sea regions, the  
140 wind forcing is usually coherent as the synoptic scale is much larger, however, the topography that is  
141 mostly not flat could generate barotropic waves at various places, and thus significantly decrease  
142 coherence of inertial currents in the lower layer.

143 The spectra of velocities in the inertial band are almost uniform except near the land boundaries (Fig. 5),  
144 consistent with the velocities. Near the boundaries, the inertial energy declines gradually to zero from  
145  $x \sim 20$  km to the land. The east side has slightly greater inertial energy and a slight wider boundary layer  
146 compared to the west side.

147 We calculate the nonlinear and inertial terms in the momentum equation and find that nonlinear terms  
148 are of significantly high values initially within 2 km away from the land boundary (Fig 6bc), where the  
149 inertial term is weak (Fig 6a). For the time-averaged values (Fig 6d), the vertical nonlinear term is two  
150 times more than the horizontal nonlinear term. The inertial term drops sharply near the boundary, and  
151 rises gradually with the distance away from the boundary. At  $x > 15$  km, it keeps an almost constant value  
152 which is much greater than nonlinear terms. Thus it is concluded that the significant decrease of inertial  
153 oscillations near the boundary is due to influence of nonlinear terms, especially the vertical nonlinear  
154 term.

#### 155 **4. Near-inertial internal waves**

156 In addition to inertial oscillations, near-inertial internal waves are usually generated along when the  
157 vertical stratification is present. However, due to their close frequencies, inertial oscillations and near-  
158 inertial internal waves are difficult to be separated. Thus we run a second simulation with the presence  
159 of stratification to investigate the differences that near-inertial internal waves introduce.

##### 160 **4.1 Temperature distributions**

161 Fig. 7 shows the evolution of temperature profiles with time. One can see an internal wave packet is

162 generated at the west coast, and then propagates offshore. The wave phase speed is about 1 km/h, close  
163 to the theoretical value (1.4 km/h). Before the arrival of internal waves, the temperature at mid-depth  
164 diffuses gradually due to vertical diffusion in the model. For a fixed position at  $x=20$  km (Fig. 8), the  
165 temperature varies with the inertial period (34.9 hours) and the amplitude of fluctuation declines  
166 gradually with time. At  $x=60$  km and  $x=100$  km, the strength of internal waves is much reduced. And  
167 wave periods are shorter initially, followed by a gradually increase to the inertial period. At  $x=140$  km,  
168 the internal wave becomes as weak as the background disturbance.

169 A spectral analysis of the temperature at mid-depth ( $z=-30$  m) is shown in Fig. 9a. The strongest peak is  
170 at near the inertial frequency (0.69 cpd), but only confined to the region close to the boundary ( $x<40$  km).  
171 In the region  $20\text{km}<x<70\text{km}$ , the energy is also large at higher frequencies of 0.8-1.7 cpd. This generally  
172 agrees with properties of Poincaré waves. During Rossby adjustment, the waves with higher frequencies  
173 propagate offshore at greater group speeds, thus for places further offshore the waves have higher  
174 frequencies (Millot and Crepon, 1981). While the wave with a frequency closest to the inertial frequency  
175 moves at the slowest group velocity, and it takes a relatively long time to propagate far offshore, thus it  
176 is mostly confined to near the boundary. By solving an idealized two-layer model equation, the response  
177 of Rossby adjustment can be expressed in form of Bessel functions (Millot and Crepon, 1981; Gill, 1982;  
178 Pettigrew, 1981), as in Fig. 9cd showing the spectra of mid-depth elevation. The difference from our case  
179 is obvious. The frequency of theoretical near-inertial waves increase gradually with the distance from the  
180 coast, while in our case this property is absent. And the theoretical inertial energy has a e-folding scale  
181 of 54 km, while in our case the e-folding scale is much smaller ( $\sim 15$  km).

## 182 **4.2 Velocity distributions**

183 With presence of near-inertial internal waves, the contours of velocities near the thermocline tilt slightly  
184 (Fig. 10d), and indicates an upward propagation of phase, thus a downward energy flux. This can also be  
185 seen in vertical spirals of velocities (Figs. 10e and 10f). With only inertial oscillations, current vectors  
186 mostly point toward two opposite directions (Figs. 10b and 10c). Once the near-inertial wave is included,  
187 the current vectors gradually rotate clockwise with depth.

188 The spatial distribution of the near-inertial energy is also slightly changed compared to the case with only  
189 inertial oscillations (Fig. 11 and Fig. 5). It is also greatly reduced to zero in the boundary layer (0-20 km)

190 like the case without stratification. But at ~50 km away from the boundary the inertial energy reaches a  
191 peak. Further away (>100 km) it becomes a constant. This spatial distribution of inertial energy is similar  
192 to that observed in shelf seas, with a maximum near the shelf break (Chen et al., 1996; Shearman, 2005).  
193 In our case, the boundary layer effect which induces a sharp decrease to zero makes a major contribution,  
194 and near-inertial internal waves which bring a small peak further offshore have a secondary influence.

## 195 **5. Dependence on the water depth**

196 In coastal regions, near-inertial motions are rarely reported. It is speculated that the strong dissipation  
197 and bottoms friction in coastal region suppress the development of near-inertial motions. However, Chen  
198 (2014) found the water depth is also a sensitive factor, with significant reduction for the case with smaller  
199 water depth. Here we will run cases with different water depths and clarify why the near-inertial energy  
200 changes with water depth. Homogeneous cases with water depths of 50 m, 40 m, 30 m, 20 m are  
201 simulated. The vertical model resolution for all cases is 1 m. All the other parameters including  
202 viscosities are the same as the homogeneous case of 60 m.

203 For each case, the currents are band-pass filtered to obtain near-inertial currents. Then near-inertial  
204 kinetic energy can be calculated. As seen in Fig. 12, the near-inertial energy gradually declines with  
205 decreasing water depth. In this dynamical system, the other dominant process is the seiches induced by  
206 barotropic waves. As the elevation induced by seiches is anti-symmetric in such a basin, the potential  
207 energy is little. The kinetic energy of seiches can also be calculated by the band-pass filtered currents.  
208 We find the energy of seiches, by contrast, increases gradually with decreasing water depth. For the case  
209 of 60 m, the near-inertial energy is much greater than the seiche energy. But for the case of 20 m, the  
210 energy of seiches has exceeded the near-inertial energy slightly. The total energy of these two processes  
211 almost keeps constant for all cases. For a shallower water depth, the reduction of near-inertial energy  
212 equals to the increase of seiche energy. The initial current is wind-driven and only distributes in the  
213 surface layer. The unbalanced across-shelf flow generates elevation near the land boundary which  
214 propagates offshore as barotropic waves and form seiches. Part of the energy goes to form inertial  
215 oscillations. For a shallower water depth, the elevation is enlarged, and more energy is transferred to  
216 form seiches, thus with weakened near-inertial motions. Therefore, in coastal regions with water depth  
217 less than 30m, the near-inertial motion is weak, due to the suppression of barotropic waves.



218 As seen in Section 3.1, inertial oscillations behave in a two-layer structure, with currents in the upper  
219 layer in opposite phase with those of lower layer. In terms of kinetic energy, for the case of 60 m (Fig.  
220 13), the near-inertial motion is maximized in the very surface, minimized near the depth of 20 m, and  
221 then gradually increases with depth to form a much smaller peak at 40 m. Near the bottom, the near-  
222 inertial energy gradually reduces to zero due to bottom friction. When we set the bottom boundary  
223 condition from nonslip to slip, such a boundary structure vanishes, and near-inertial energy become  
224 constant in the lower layer. For other cases of 20 m and 40 m, their vertical profile are almost the same  
225 as the 60 m case. The minimum positions are all located at  $1/3$  of the water depth. This implies the  
226 vertical distribution of near-inertial energy is independent of water depth. Note that in our cases, the  
227 vertical viscosity is set as a constant value. In practice, the viscosity in the thermocline is usually  
228 significantly reduced, thus the minimum position of near-inertial energy is located just below the mixed  
229 layer.

## 230 **6. Summary and discussion**

231 Idealized simple two-dimensional ( $x$ - $z$ ) simulations are conducted to examine the response of a shallow  
232 closed basin to a wind pulse. The first case is homogeneous, in which the near-inertial motion is a pure  
233 inertial oscillation. It has a two-layer structure, with currents in the surface and lower layers being  
234 opposite in phase, which has been reported frequently in shelf seas. We find that the inertial current is  
235 confined in the surface layer initially. The induced depth-integrated transport generates barotropic waves  
236 near the boundaries which propagates quickly offshore. The flow driven by the barotropic wave is  
237 independent of depth and opposite to the surface flow. Thus the surface flow is reduced but the flow in  
238 the lower layer is increased, as a result the transport diminishes. This feedback between barotropic waves  
239 and currents continues and ends up with the depth-integrated transport vanishing, i.e., inertial currents in  
240 the upper and lower layers having opposite phases and comparable amplitudes. In our simulation, within  
241 just one inertial period the typical structure of inertial currents has been established. By solving a two-  
242 layer analytic model using the Laplace transform, Pettigrew (1981) also found the vertical structure of  
243 opposite currents associated with inertial oscillations. He argued that the arrival of a barotropic wave for  
244 a fixed location cancels half of the inertial oscillation in the surface layer, and initiates an equal and  
245 opposite oscillation in the lower layer. However, in our simulation the arrival of the first barotropic wave  
246 cannot cancel half of the surface flow. The balanced state of upper and lower flows takes more time to

247 reach.

248 The second case is a setup with idealized two-layer stratification, thus near-inertial internal waves are  
249 generated. For a fixed position, velocity contours show obvious tilting near the thermocline, and velocity  
250 vectors display clearly anti-cyclonic spirals with depth. These could be useful clues to examine  
251 occurrence of near-inertial internal waves. Near the land boundary the vertical elevation generates  
252 fluctuations of thermocline that propagate offshore. The energy of near-inertial internal waves is confined  
253 to near the land boundary ( $x < 40$  km). At positions further offshore, the waves have higher frequencies.  
254 This is generally consistent with properties of a Rossby adjustment process. However, our simulated  
255 results also show evident discrepancies from theoretical values obtained in the classic solutions of Rossby  
256 adjustment problem. These discrepancies are probably attributed to nonlinearity of the model, and the  
257 changing stratification in the model due to diffusion and mixing, compared to constant density difference  
258 between two layers in theoretical cases.

259 The inertial oscillation has a very large coherent scale of almost the whole basin scale. It is uniform in  
260 both amplitude and phase across the basin, except near the boundary ( $\sim 20$  km offshore). The energy of  
261 inertial oscillations declines gradually to zero from  $x = 20$  km to the coast. This boundary effect is  
262 attributed to the influence of nonlinear terms, especially the vertical term ( $w \partial \mathbf{u} / \partial z$ ), which are greatly  
263 enhanced near the boundary, and overweighs the inertial term ( $f \mathbf{u}$ ). When near-inertial internal waves  
264 are produced in the stratified case, the distribution of total near-inertial energy is modified slightly near  
265 the boundary. A small peak appears at  $\sim 50$  km offshore. This is similar to the cross-shelf distribution of  
266 near-inertial energy observed in shelf seas (Chen et al., 1996; Shearman, 2005). This energy distribution  
267 has been attributed to downward and offshore leakage of near-inertial energy near the coast (Kundu et  
268 al., 1983), the variation of elevation and Reynolds stress terms associated with the topography (Chen and  
269 Xie, 1997) and the influence of the baroclinic wave (Shearman, 2005; Nicholls et al., 2012). In our  
270 simulations, this horizontal distribution of near-inertial energy is primarily controlled by the boundary  
271 effect on inertial oscillations, and the near-inertial internal wave has a secondary effect.

272 Homogeneous cases with various water depths (50 m, 40 m, 30 m, and 20 m) are also simulated. The  
273 inertial energy is reduced with decreasing water depth, while the energy of seiches, by contrast, is  
274 increased. For the case of 20 m, the seiche energy has slightly exceeds the inertial energy. It is interesting  
275 that the reduction of inertial energy just equals the increase of the seiche energy, which implies more

276 energy of initial wind-driven currents is transferred to the seiches for the shallower cases, and thus less  
277 energy goes to the inertial process. This is probably an important reason why near-inertial motions are  
278 weak and rarely reported in shallow coastal regions.

279

280

281

## 282 **Acknowledgements**

283 We are appreciated for discussions with John Huthnance and comments from the editor and reviewers.  
284 This study is supported by the National Basic Research Program of China (2014CB745002,  
285 2015CB954004), the Shenzhen government (201510150880, SZHY2014-B01-001), and the Natural  
286 Science Foundation of China (U1405233). Shengli Chen is sponsored by the China Postdoctoral Science  
287 Foundation (2016M591159).

288

289

290

## 291 **References**

292 Alford, M. H., Cronin, M. F., and Klymak, J. M.: Annual Cycle and Depth Penetration of Wind-Generated  
293 Near-Inertial Internal Waves at Ocean Station Papa in the Northeast Pacific, *Journal of Physical*  
294 *Oceanography*, 42, 889-909, 10.1175/jpo-d-11-092.1, 2012.

295 Alford, M. H., MacKinnon, J. A., Simmons, H. L., and Nash, J. D.: Near-Inertial Internal Gravity Waves in  
296 the Ocean, *Ann Rev Mar Sci*, 8, 95-123, 10.1146/annurev-marine-010814-015746, 2016.

297 Burchard, H., and Rippeth, T. P.: Generation of Bulk Shear Spikes in Shallow Stratified Tidal Seas,  
298 *Journal of Physical Oceanography*, 39, 969-985, 10.1175/2008jpo4074.1, 2009.

299 Chen, C., and Xie, L.: A numerical study of wind-induced, near-inertial oscillations over the Texas-  
300 Louisiana shelf, *Journal of Geophysical Research: Oceans*, 102, 15583-15593, 10.1029/97jc00228,  
301 1997.

302 Chen, C. S., Reid, R. O., and Nowlin, W. D.: Near-inertial oscillations over the Texas Louisiana shelf, *J*  
303 *Geophys Res-Oceans*, 101, 3509-3524, 10.1029/95jc03395, 1996.

304 Chen, S.: Study on Several Features of the Near-inertial Motion, PhD, Xiamen University, 107 pp.,

305 2014.

306 Chen, G., Xue, H., Wang, D., and Xie, Q.: Observed near-inertial kinetic energy in the northwestern  
307 South China Sea, *J Geophys Res-Oceans*, 118, 4965-4977, 10.1002/jgrc.20371, 2013.

308 Chen, S., Hu, J., and Polton, J. A.: Features of near-inertial motions observed on the northern South  
309 China Sea shelf during the passage of two typhoons, *Acta Oceanologica Sinica*, 34, 38-43,  
310 10.1007/s13131-015-0594-y, 2015a.

311 Chen, S., Polton, J. A., Hu, J., and Xing, J.: Local inertial oscillations in the surface ocean generated by  
312 time-varying winds, *Ocean Dynamics*, 65, 1633-1641, 10.1007/s10236-015-0899-6, 2015b.

313 Chen, S., Polton, J. A., Hu, J., and Xing, J.: Thermocline bulk shear analysis in the northern North Sea,  
314 *Ocean Dynamics*, 66, 499-508, 10.1007/s10236-016-0933-3, 2016.

315 D'Asaro, E. A.: The energy flux from the wind to near-inertial motions in the surface mixed layer,  
316 *Journal of Physical Oceanography*, 15, 1043-1059, 1985.

317 Fu, L. L.: Observations and models of inertial waves in the deep ocean, *Reviews of Geophysics*, 19,  
318 141-170, 10.1029/RG019i001p00141, 1981.

319 Gill, A. E.: *Atmosphere-ocean dynamics*, Academic Press, 662 pp., 1982.

320 Gill, A. E.: On the behavior of internal waves in the wakes of storms, *Journal of Physical Oceanography*,  
321 14, 1129-1151, 10.1175/1520-0485(1984)014<1129:otboiw>2.0.co;2, 1984.

322 Kundu, P. K., Chao, S. Y., and McCreary, J. P.: Transient coastal currents and inertio-gravity waves, *Deep-*  
323 *Sea Research Part a-Oceanographic Research Papers*, 30, 1059-1082, 10.1016/0198-0149(83)90061-4,  
324 1983.

325 Leaman, K. D., and Sanford, T. B.: Vertical energy propagation of inertial waves: a vector spectral  
326 analysis of velocity profiles, *Journal of Geophysical Research*, 80, 1975-1978, 1975.

327 MacKinnon, J. A., and Gregg, M. C.: Near-inertial waves on the New England shelf: The role of evolving  
328 stratification, turbulent dissipation, and bottom drag, *Journal of Physical Oceanography*, 35, 2408-  
329 2424, 10.1175/jpo2822.1, 2005.

330 Malone, F. D.: An analysis of current measurements in Lake Michigan, *Journal of Geophysical*  
331 *Research*, 73, 7065-&, 10.1029/JB073i022p07065, 1968.

332 Marshall, J., Adcroft, A., Hill, C., Perelman, L., and Heisey, C.: A finite-volume, incompressible Navier  
333 Stokes model for studies of the ocean on parallel computers, *Journal of Geophysical Research: Oceans*,  
334 102, 5753-5766, 10.1029/96jc02775, 1997.

335 Millot, C., and Crepon, M.: Inertial oscillations on the continental-shelf of the Gulf of Lions -  
336 observations and theory, *Journal of Physical Oceanography*, 11, 639-657, 10.1175/1520-  
337 0485(1981)011<0639:iotcs>2.0.co;2, 1981.

338 Nicholls, J. F., Toumi, R., and Budgell, W. P.: Inertial currents in the Caspian Sea, *Geophysical Research*  
339 *Letters*, 39, 10.1029/2012gl052989, 2012.

340 Pettigrew, N. R.: *The dynamics and kinematics of the coastal boundary layer off Long Island*, 1981.

341 Pollard, R. T., and Millard, R. C.: Comparison between observed and simulated wind-generated inertial  
342 oscillations, *Deep Sea Research*, 813-821, 1970.

343 Price, J. F.: Upper ocean response to a hurricane, *Journal of Physical Oceanography*, 11, 153-175,  
344 10.1175/1520-0485(1981)011<0153:uortah>2.0.co;2, 1981.

345 Shearman, R. K.: Observations of near-inertial current variability on the New England shelf, *Journal of*  
346 *Geophysical Research*, 110, 10.1029/2004jc002341, 2005.

347 Sun, Z., Hu, J., Zheng, Q., and Li, C.: Strong near-inertial oscillations in geostrophic shear in the  
348 northern South China Sea, *Journal of Oceanography*, 67, 377-384, 10.1007/s10872-011-0038-z, 2011.

349 Webster, F.: Observation of inertial period motions in the deep sea, *Reviews of Geophysics*, 6, 473-  
350 490, 1968.

351 Xing, J. X., Davies, A. M., and Fraunie, P.: Model studies of near-inertial motion on the continental  
352 shelf off northeast Spain: A three-dimensional two-dimensional one-dimensional model comparison  
353 study, *J Geophys Res-Oceans*, 109, 10.1029/2003jc001822, 2004.

354 Zheng, Q., Lai, R. J., and Huang, N. E.: Observation of ocean current response to 1998 Hurricane  
355 Georges in the Gulf of Mexico, *Acta Oceanol. Sin.*, 25, 1-14, 2006.

356

357

358

359

360

361

362

363

364

365

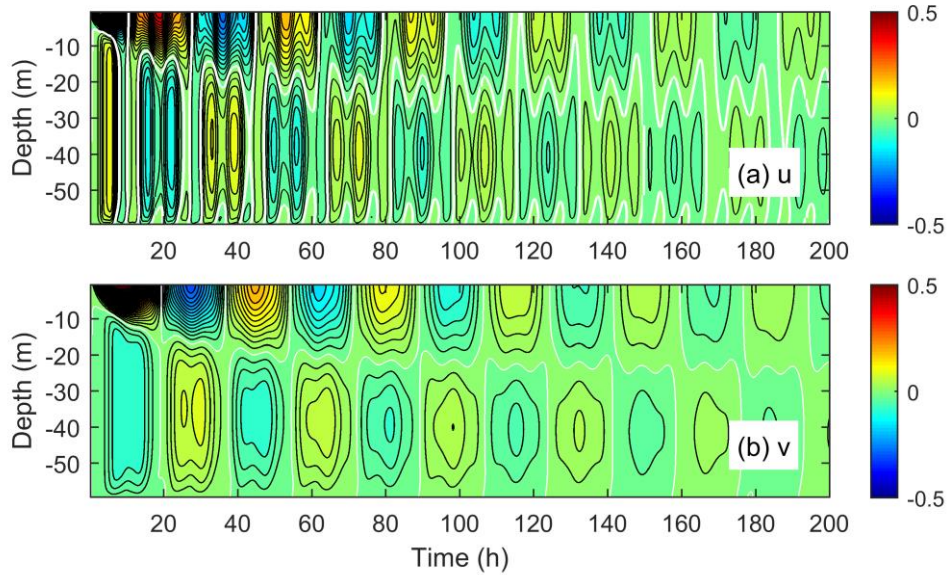
366

367

368

369 **Figures**

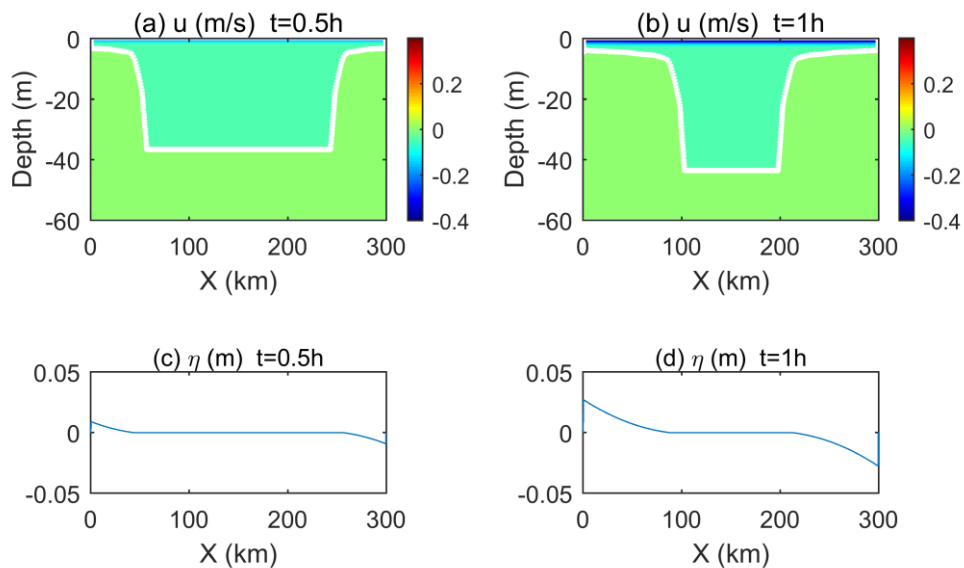
370



371

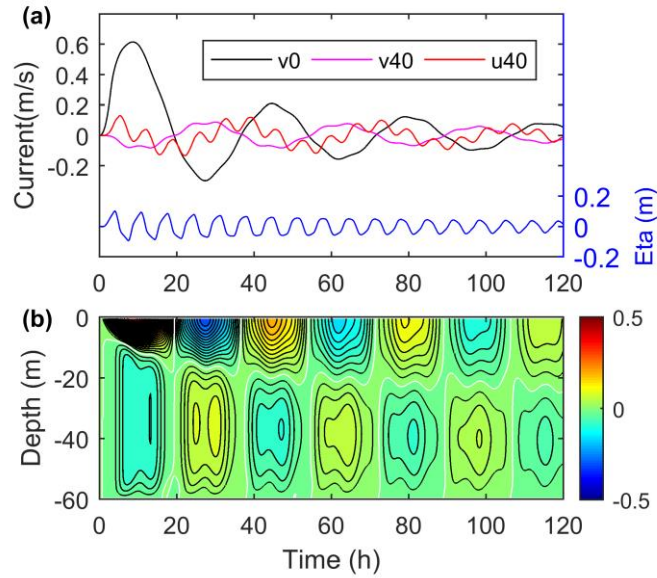
372 Fig. 1 Velocities ( $u$  and  $v$ , m/s) at  $x=70$  km. The white lines denote the value of zero. The contour  
373 interval is 0.02 m/s for both panels.

374



375

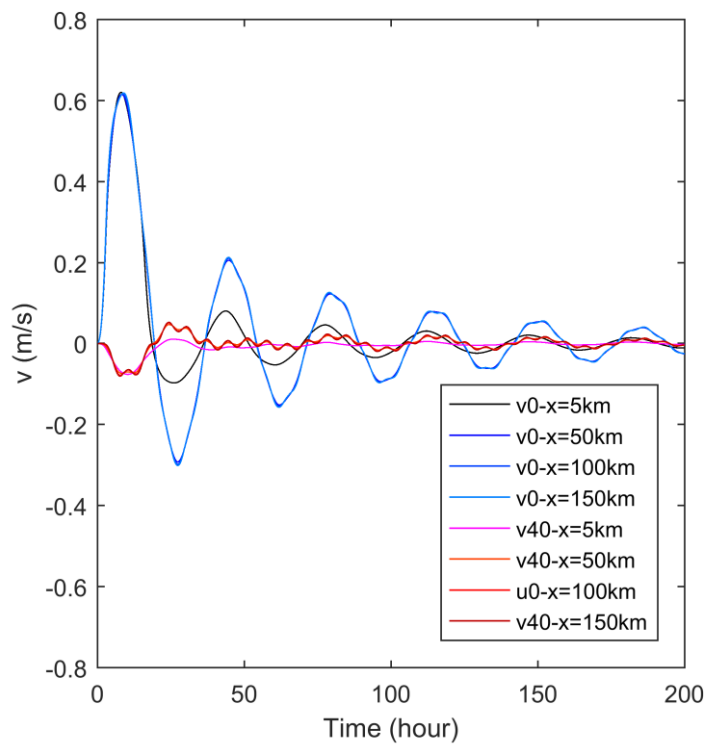
376 Fig. 2 Snapshots of eastward velocity and elevation ( $\eta$ ) at  $t=0.5$  and 1 hour. The white lines represent  
377 the value of zero.



378

379 Fig. 3 (a) Time series of velocities and elevation at  $x=100$  km. 'v0' and 'v40' mean the northward  
 380 velocity ( $v$ ) at depths of 0 m and 40 m, and 'u40' is the eastward velocity ( $u$ ) at 40 m. (b) Contours of  $v$   
 381 at  $x=100$  km. The white lines denote the value of zero, and the contour interval is 0.02 m/s.

382



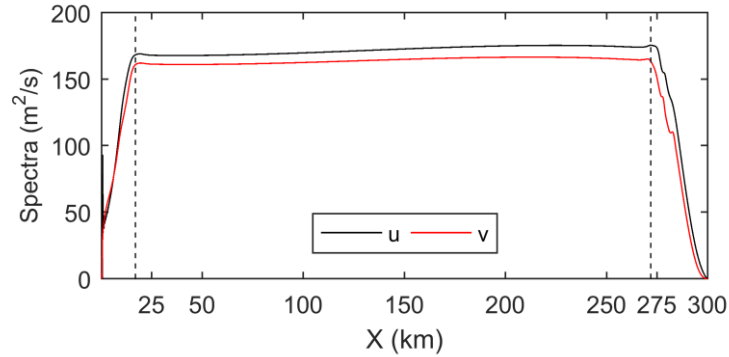
383

384 Fig. 4 Time series of the northward velocity ( $v$ ) at different depths and positions. 'v0' and 'v40' mean  $v$

385

at depths of 0 m and 40 m.

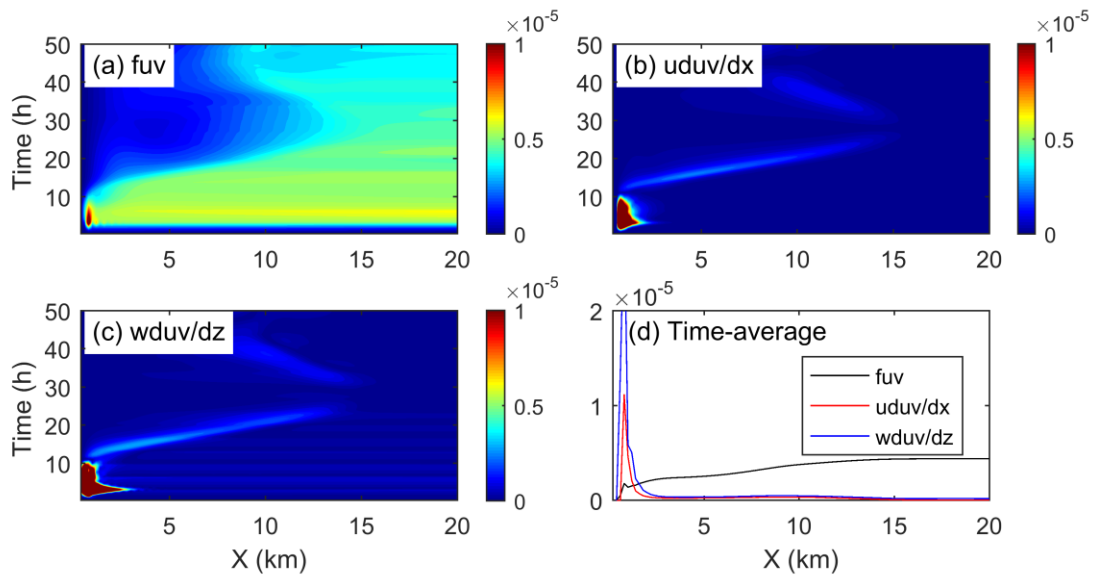
386



387

388 Fig. 5 Spatial variation of depth-mean near-inertial spectra of velocities for the homogeneous case.

389



390

391 Fig. 6. Variation of depth-mean inertial and nonlinear terms ( $\text{m/s}^2$ ). The inertial term (a) is calculated as

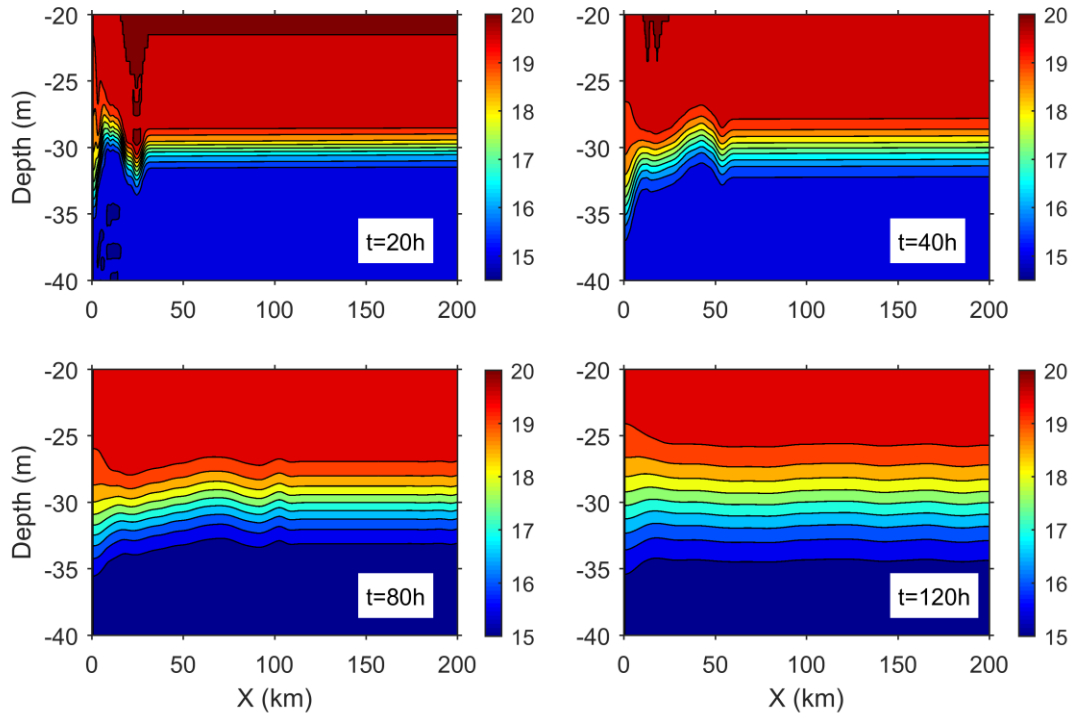
392  $|f(u + iv)|$ , the horizontal nonlinear term (b) is  $|u(\partial u / \partial x + i\partial v / \partial x)|$ , and the vertical nonlinear

393 term (c) is  $|w(\partial u / \partial z + i\partial v / \partial z)|$ . (d) Time averaged value for the first 50 hours.

394

395

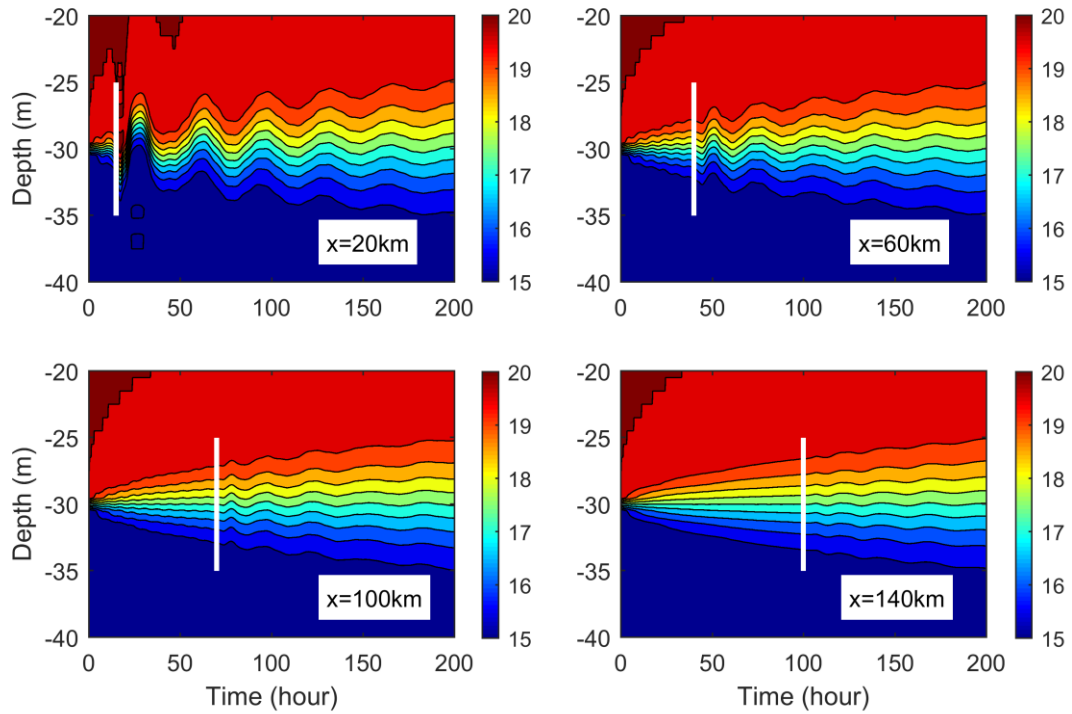




396

397 Fig. 7 Snapshots of temperature profiles at  $t=20h$ ,  $40h$ ,  $80h$  and  $120h$ . The contour interval is  $0.5\text{ }^{\circ}\text{C}$ .

398

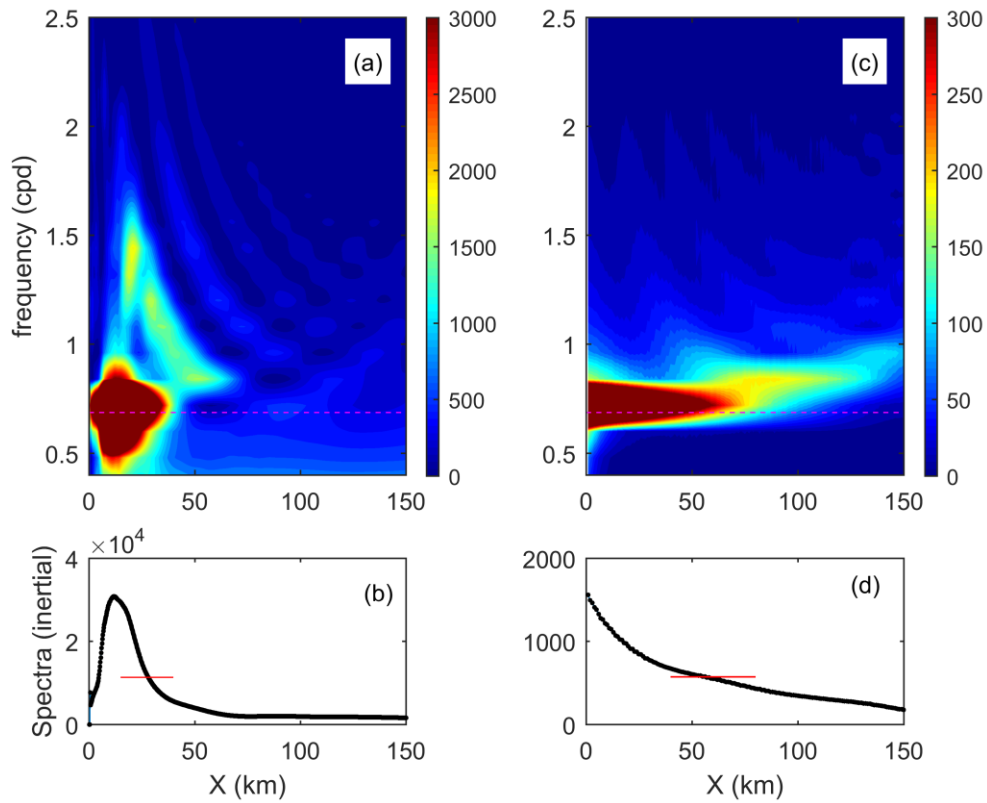


399

400 Fig. 8 Time series of temperature at  $x=20$ ,  $60$ ,  $100$  and  $140$  km. White lines denote the arrival of

401

internal waves. The contour interval is  $0.5\text{ }^{\circ}\text{C}$ .

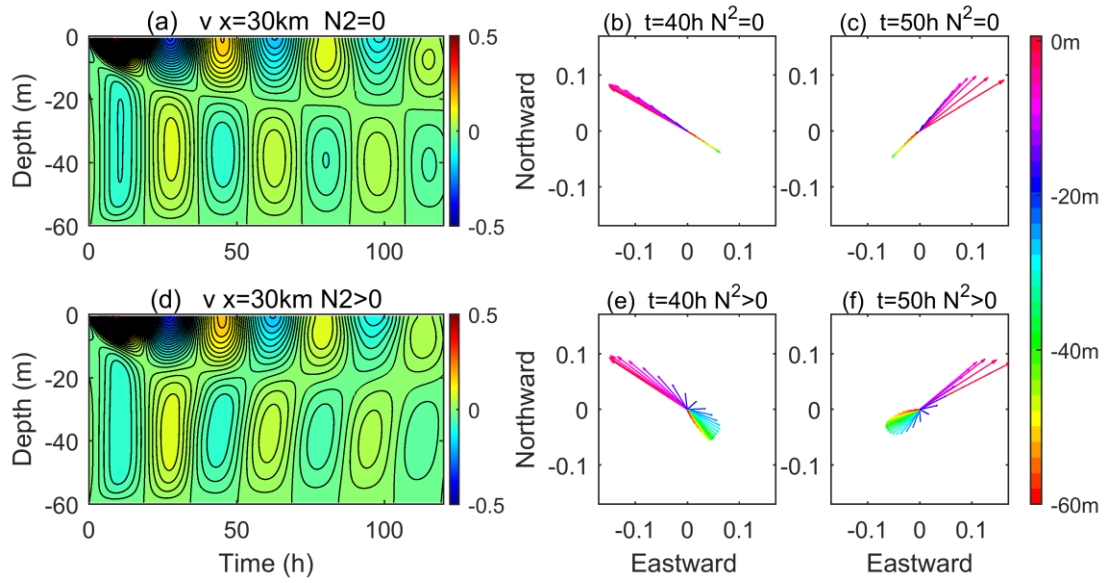


403

404 Fig. 9 (a) Spectra of the temperature at the mid-depth ( $z = -30$  m). The pink dash line represents the  
 405 inertial frequency. (b) Sum of spectra in inertial band with a red line denoting the e-folding value of the  
 406 peak. (c) Theoretical spectra of mid-depth elevation calculated from the solution in the form of a Bessel  
 407 function as in Eq. 3.16 of Pettigrew (1981). (d) Same as (b) but for theoretical spectra.

408

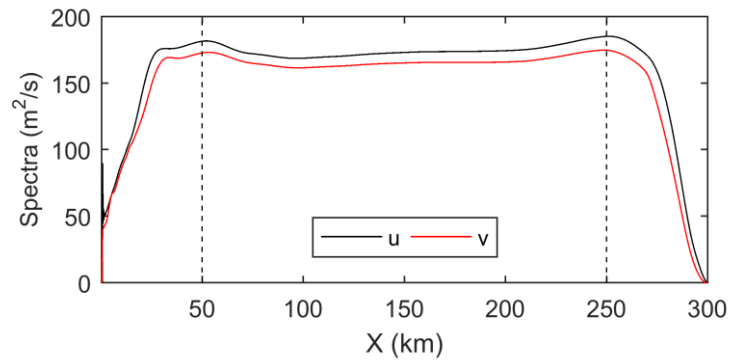
409



410

411 Fig. 10 Distribution of near-inertial currents ( $v$ , m/s) and current spirals for the cases without (a, b, c)  
 412 and with (d, e, f) stratification at  $x=30$  km. The near-inertial currents are obtained by applying a band-  
 413 pass filter. The contour interval is 0.02 m/s.

414

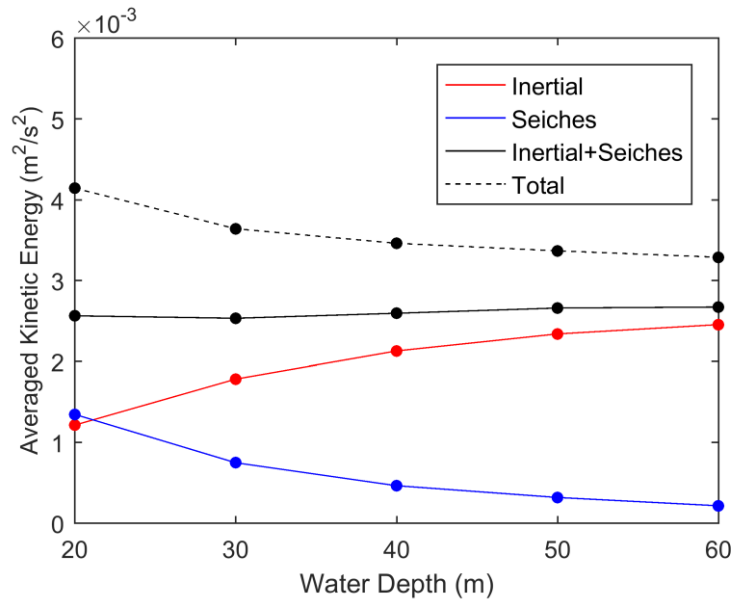


415

416 Fig. 11 Spatial variation of depth-mean near-inertial spectra of velocities for the stratified case.

417

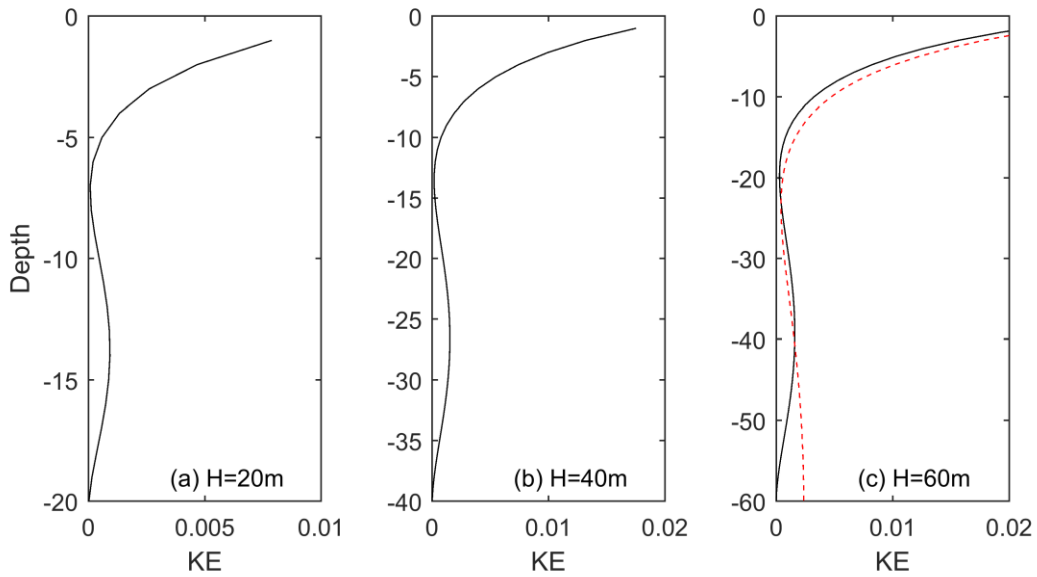
418



419

420 Fig. 12 The kinetic energy of near-inertial motions and seiches for different water depths. For each  
 421 case, the currents are ban-pass filtered to get currents for each type of motions which are then averaged  
 422 over time and integrated over space to obtain a final value.

423



424

425 Fig. 13 Vertical profile of averaged inertial kinetic energy for the homogeneous cases with water depths  
 426 of 20 m, 40 m and 60 m. The red dash line in (c) denotes the slip case.